Atomically Unveiling an Atlas of Polymorphisms in Transition Metal Trihalides

Xiaocang Han[†,‖], *Jing-Yang You*[‡,‖], *Shengqiang Wu*[†], *Runlai Li*[§], *Yuan Ping Feng*[‡], *Kian Ping Loh*[⊥,*], *Xiaoxu Zhao*[†,*]

[†]School of Materials Science and Engineering, Peking University, Beijing 100871, China

[‡] Department of Physics, National University of Singapore, 2 Science Drive 3, 117551, Singapore

[§]College of Polymer Science & Engineering, State Key Laboratory of Polymer Materials Engineering, Sichuan University, Chengdu, 610065, China

[⊥]Department of Applied Physics, Hong Kong Polytechnic University, Hung Hom, Hong Kong SAR

[‖]These authors contributed equally to this work

Correspondence and requests for materials should be addressed to K. P. L (kploh@polyu.edu.hk) & X. X. Z (xiaoxuzhao@pku.edu.cn)

Abstract:

Transition metal trihalides MX_3 (M=Cr, Ru; X=Cl, Br, and I) belong to a family of novel 2D magnets that can exhibit topological magnons and electromagnetic properties, thus affording great promises in next-generation spintronic devices. Rich magnetic ground states observed in the MX_3 family are believed to be strongly correlated to the signature Kagome lattice and interlayer van der Waals (vdW) coupling raised from distinct interlayer stacking orders. However, the intrinsic air instability of the MX_3 family makes their direct atomic-scale analysis challenging. Therefore, information on the stacking registry-dependent-magnetism for various MX_3 remains elusive, which greatly hinders the engineering of the desired phase. Here, we report a completely non-destructive transfer method, and successfully realize a one-

step intact transfer of bilayer MX$_3$ films, as evidenced by scanning transmission electron microscopy (STEM). After surveying hundreds of MX$_3$ thin flakes, we provide a full spectrum of stacking orders in the MX$_3$ family with atomic precision and calculated their associated magnetic ground states, unveiled by combined STEM and density functional theory (DFT). In addition to well-documented phases, we discover a new monoclinic C2/c phase widely existing in most MX$_3$. Besides, a high density of strain soliton boundaries is consistently found in all MX$_3$, allowing FM-rhombohedral to AFM-monoclinic stacking transitions in CrI$_3$. Therefore, our study sheds light on the the structural basis of the diverse magnetic orders in MX$_3$, paving the way for modulating magnetic couplings via stacking engineering.

INTRODUCTION

Since the discovery of intrinsic long-range magnetic order in atomically-thin van der Waals (vdW) crystals, two-dimensional (2D) vdW magnetic materials have attracted significant attention for their exceptional performance in magnetic spintronic and magnetoelectric devices.[1–5] Notably, MX$_3$ (M = Cr, Ru; X=Cl, Br, and I) is a crucial member of 2D magnets with intriguingly tunable magnetic properties,[6] such as large tunneling magnetoresistance,[7,8] spin liquid,[9,10] topological magnons,[11,12] electron-phonon coupling,[13] which have great prospects in spin-filter magnetic tunnel junction,[14,15] non-volatile memory,[16] spin valve,[17] spintronic and magnonic applications.[18]

Intrinsically rich magnetic orders inherited in the MX$_3$ family can be further precisely modulated by electric gating,[19] pressure,[20] electrostatic doping,[21] stacking registry,[22] etc. The essence of triggering such magnetic order modulation is to change the interlayer vdW coupling.[19–22] In addition to introducing an external force to control the vdW coupling, a more natural and generic way is to create different stacking arrangements via interlayer sliding or rotating. For example, there are two representative phases in CrI_3, *i.e.*, antiferromagnetic (AFM) monoclinic (space group C2/m) stacking and ferromagnetic (FM) rhombohedral (space group $R\bar{3}$) stacking registries.[23] Different FM and AFM magnetic orders have been observed in two phases due to unique M-X-X-M superexchange interaction and spin-lattice coupling stemming from distinct interlayer stacking orders.[23–25] Taking bilayer $CrBr_3$ as an example, the interlayer magnetic coupling can be either FM or AFM depending on the stacking order controlled by the interlayer twist angle and in-plane translation.[22] Therefore, stacking engineering has been demonstrated as a promising approach to tuning the magnetic properties of MX_3.

Magnetic ground states induced by interlayer gliding have been a core focus of DFT calculations in MX_3,[26,27] which is in good agreement with most experimental observations so far.[28] However, less attention has been paid to how the stacking order affect magnetic properties in 2D few-layer MX_3. The lack of knowledge on the various polymorphs and polytypes of MX_3 stems partly from the poor stability of MX_3, where rapid sample degradation in air precludes microscopic characterization.[29] Despite the absence of phase transition occurring in atomically-thin CrI_3 as verified by electron microscopy,[30] intiguing AFM-to-FM magnetic orders have been widely observed.[2,20,31] The origin of the different (AFM/FM) magnetic ground states of CrI_3 thin films remains elusive. Given a rich interplay between stacking order and interlayer exchange,[26,32,33] , the atomic-scale stacking features, and associated magnetic profiles are interesting subjects to be investigated in few-layer MX_3 crystals.

The layered vdW materials, MX_3 are a three-atom-thick sandwich-like structure analogous to 1T-phase MoS_2. The key difference from 1T-MoS_2 is that the sandwiched *M* metal layer only occupies octahedral vacancies with 66.7% occupancies created by two layers of X planes, exhibiting orderly $\sqrt{3}a \times \sqrt{3}a$ periodic metal vacancies. The structure is endowed with rich stacking polytype chemistry which differs in stacking arrangements of neighboring MX_3 slabs along the crystallographic c axis. Bulk chromium trihalides CrX_3 (X=Cl, Br, and I) are suggested to undergo temperature-dependent crystallographic phase transitions, from high-temperature monoclinic C2/m stacking to low-temperature rhombohedral $R\overline{3}$ phase with neglectable (significant) change in the intralayer (interlayer) structure[23,34–36] as verified by X-Ray diffraction and the theory[23]. The phase transition takes place near 240 K, 420 K, and 210 K in bulk CrX_3 (X=Cl, Br, and I), respectively,[36] which was not observed in few-layer CrX_3.[30,37] The layered $RuCl_3$ compounds have been reported to adopt the monoclinic C2/m phase[38] at low temperatures with a zigzag AFM structure and exhibit the trigonal $P3_112$ phase at high temperatures.[39] Given the weak interlayer vdW coupling,[2] there is a tendency to form stacking faults and metastable polytypes, owing to their very similar formation energies with the normal phase.[10,40] Other than the most commonly observed C2/m and $R\overline{3}$ phases, other interesting stacking polytypes with intriguing physical properties remain to be explored. In addition, most of the recently reported MX_3 suffer from a fundamental obstacle, *i.e.,* instability under air conditions, which severely hinders the structural characterization of MX_3 with atomic precision.[41]

Here, we employed a completely dry transfer method to transfer atomically-thin MX_3 crystals (Figure S1) for atomic-scale observations inside the glove box. Using atomic-resolution annular dark field-scanning transmission electron microscopy (ADF-STEM) and image simulation, an atlas of stacking polytypes, including the newly discovered C2/c phase, have been atomically identified, and their associated magnetic orders are further predicted by DFT calculations. The C2/c monoclinic stacking has similar formation energy with C2/m in the few-layer CrI_3 and coexist, whereas $P3_112$ and $R\overline{3}$ phases are less common. Analogous to the C2/m phase, the C2/c polytypes reveal an AFM structure. On the other hand, $P3_112$, and $R\overline{3}$ phases illustrate distinct magnetic couplings in different MX_3. After counting over few hundreds crystals, we found that four different MX_3 exhibit unique stacking polytypes distributions, paving an alternative way to design spintronic devices with desirable magnetic properties by switching the stacking structures in the same vdW 2D magnet.

RESULTS AND DISCUSSIONS

The dry-stamp transfer method was employed to produce atomically thin and clean 2D flakes suitable for atomic-resolution STEM imaging,[42] especially for the MX_3 crystals sensitive to air, light, and/or moisture. As illustrated in Figure 1a, the mechanically exfoliated thick MX_3 flakes prepared in an inert argon glovebox were further exfoliated by polydimethylsiloxane (PDMS), and then dry-transferred onto a targeted Cu Quantifoil grid after removing PDMS by mild heating, leaving few-layer flakes suspended over the holes of the support STEM grid. Figure 1b shows the atomic-scaled STEM images of successfully transferred $CrBr_3$, where the local thickness is down to bilayers, as corroborated by the simulated image. This dry transfer method also applies to the air-sensitive CrI_3. It can be seen that the atomic structure of the CrI_3 flake remains intact and homogeneous even along the edge region without substantial degradation (Figure 1c). Interestingly, the atomically sharp edge is highly faceted, preferring to terminate along the $\{33\overline{1}\}$ planes of the crystal (Figure 1c). In 2D layered MX_3, the M ions in each layer are arranged in a honeycomb network with distorted edge-sharing octahedral coordination by six X ions (Figure 1d). On the basis of the atomic structure of monolayer MX_3 (point group, D_{3d}), there are nine possible interlayer stacking sites per unit cell if only staggered or eclipsed configurations were considered, *i.e.,* labeled by *A*, *B*, *C*, *D*, *E*, *F*, *G*, *H*, and *I* (Figure 1d, right panel), so that the *M* in the top layer could be directly stacked over the center of a hole (*A*), two Cr (*B*, *F*) or six *X* (*C*, *D*, *E*, *G*, *H*, *I*) positions in the bottom layer. The basis vectors ***a*** and ***b*** (purple lines) are along the zigzag directions, whereas the armchair directions are marked by cyan lines in the monolayer framework (Figure 1d). Beyond monolayer, the stacking phases of layered MX_3 involve interlayer gliding to change their relative positions upon stacking sequences (Figure 1e), *e.g.*, *AB* (zigzag direction [010]) or *FB* (armchair direction [210]).

To unravel the atomic structure of stacking polytypes in few-layered MX_3 crystals, an aberration-corrected ADF-STEM was employed to characterize the as-transferred atomically-thin MX_3 samples. Representative atomic-resolution ADF-STEM images of CrI_3 taken along the *c* axis at room temperature are illustrated in Figure 2e-2h. The intensity of an atomic column in ADF-STEM images is roughly proportional to $\sim Z^{1.6\text{-}1.9}$, where Z denotes the atomic number.[43,44] The periodic intensity variations in these STEM images indicate different ordering sequences. Therefore, based on different projected 2D intensity maps shown in ADF-STEM images (Figure 2e-2h), the crystal structures of atomically-thin CrI_3 can be unambiguously classified into four distinct stacking types: (1) the C2/m monoclinic stacking; (2) the C2/c monoclinic stacking; (3) the $P3_112$ trigonal stacking; and (4) the $R\overline{3}$ rhombohedral phase. The layer arrangements of the Cr framework for the four phases with one period are shown in Figure 2a-2d. The atomic-level consistency between the experimental image and its simulation (Figure 2e-2h) derived from the DFT optimized structural models of CrI_3 unambiguously demonstrates that the ADF-STEM is reliable for directly differentiating the polytypes and local topological defects in 2D materials.

Atomic-level phase identifications

As reported by McGuire,[23] there are two representative phases in bulk CrI_3, *i.e.,* rhombohedral ($R\bar{3}$) and monoclinic (C2/m) phases. The C2/m monoclinic (ABC) stacking can be uniquely identified by the top-view atomic-resolution images revealing a signature stripy pattern in which each layer glides sequentially along the zigzag direction by $1/3a$ fractional unit cell (Figure 2b). The well-defined striped topology can be directly visualized by STEM images exhibiting a triple-striped structure. The lattice arrangements of the C2/c phase (Figure $2e^{ii}$) display a triple-stripe in which the center line has one bright line, and the other two lines are relatively weaker. The situation, however, is different in the C2/m structure (Figure $2f^{ii}$), whereas every third line substantially darker than the other two (Figure $2f^{ii}$).[29,45] It is worth noting that in the C/2m phase the darker line contains only I_2-hollow atomic columns and two bright lines are composed of mixed Cr-I_2 (Figure S2). The intensity variation and periodic ordering can be seen clearly in the intensity line profiles (Figure $2e^{iii}$, $2f^{iii}$). These contrast variations can be well explained by the stacking differences between the two phases. Notably, the striped patterns can be observed in almost all CrI_3 few-layers in this study (Figure 2k), indicating that it is the energetically preferred phase, which is consistent with our calculations in later section. To the best of our knowledge, the specific structural periodicity of the the monoclinic C2/c phase in CrI_3 has not been observed in either exfoliated or chemically produced MX_3 materials before.

To precisely distinguish the stacking difference between these two monoclinic phases, we statistically analyzed the intensity of all atom sites in STEM images (see Figure S3). The corresponding histograms of the intensity distribution of two monoclinic structures are shown in Figure $2e^{iv}$ and $2f^{iv}$, respectively. Notably, the intensity distribution is divided into three peaks in C2/m (Figure $2f^{iv}$), whereas there are only two significant peaks in C2/c stacking (Figure $2e^{iv}$). Based on the Z-contrast ADF-STEM image, we can deduce that the striped structure shown in

Figure 2e exhibits a C2/c monoclinic stacking, confirmed by the simulated image (Figure 2e^{ii}, bottom panel). The C2/c three-step staircase pattern contains six layers in one unit cell, which can be decomposed into the zigzag stacks of -A-D-B-E-C-F- as illustrated in the atomic model (Figure 2a). The regular intensity feature (Figure 2e^{iv}) suggests that the stacking sequence of C2/c is definite, otherwise that will result in irregular image contrast since the layer number is changeable. The stacking of -D-, -E-, -F- are similar to the -A-, -B-, -C-, but they glide relatively along the other degenerate zigzag direction by 1/3*a* fractional unit cell (Figure 2a). The stripe contrast is caused by the alignment of Cr-I_2 positioned on the Cr-I_2 (bright stripes) or I_2-hollow (dark stripes) sites in adjacent layers, as indicated by $\{Cr_2I_4\}$ and $\{CrI_4\}$, respectively. The frequency of bright spots caused by additional Cr atoms is statistically half the frequency of dark spots in the lattice, indexing the stoichiometric ratio of CrI_3. Besides, the simulated intensity line profiles (Figure 2e^{iii}) agree well with the experimental results, reconfirming the C2/c stacking sequence.

In addition, a structural distortion induced by the periodic in-plane Cr-I bond contraction and elongation from ideal monoclinic symmetry (*i.e.*, undistorted CrI_6 octahedron) was observed in multilayer C2/c and C2/m crystals (Figure 2e^{ii}, 2f^{ii}). Two bright CrI_2 mixed lines keep away from the dark I_2 line (2.2 Å) in C2/m, while the columns of $\{CrI_4\}$ dark lines move towards bright $\{Cr_2I_4\}$ columns lines (1.9 Å) in C2/c. The resulting deviation of the Cr-I bonds leads to a distorted octahedral symmetry, which was further corroborated by the DFT-optimized structure, and is robust against the stacking registry and interlayer coupling ((Figure S4, S5). Furthermore, the observation of the monoclinic phases with lattice distortion suggests a real-space atomic-level evidence for distorted octahedra in MX_3, which is vital to the resultant magnetic ground state as it is highly sensitive to the local geometry.[39,46]

Besides monoclinic phases, we also found the R$\bar{3}$ (Figure 2d, *BFG*) rhombohedral stacking (Figure 2h^{i}), commonly denoted as low temperature phase, and it only exists as a tiny fraction (~5%) after counting over hundred atomically-thin CrI_3 flakes (Figure 2k). As shown in Figure 2h^{ii}, the atom arrangements of R$\bar{3}$ phase illustrates a signature hexagon-shaped periodic bright spots with one dark spot in the middle of a hexagon, confirmed by the consistency with the simulated image (Figure 2h^{ii}, bottom panel). The low population of the R$\bar{3}$ phase suggests that it is not energetically favorable at room temperature. Interestingly, an unusual periodic structure, different from the above-mentioned rhombohedral and monoclinic stackings, can be observed in few-layer CrI_3 (Figure 2g^{i}). The periodic structure (Figure 2g^{ii}) consists of a repetition of one unit cell containing six bright spots (marked by a white dashed line) and three less bright spots (marked by a yellow dashed line), similar to the observed $P3_112$ phase in α-$RuCl_3$ thin film.[39] Besides, the simulated image (Figure 2g^{ii}, bottom panel) from the $P3_112$ atomic model agrees well with the experimental results, confirming the $P3_112$ (Figure 2c, *ABD*) stacking sequence. As expected, the bright spots are assigned to Cr-I_2 atoms columns, while the dark one is I_2-hollow atomic columns, producing a specific repeating pattern in $P3_112$ trigonal symmetry. In addition, a relative displacement (7.2%) marked by white arrows was observed in the positions of iodine columns, consistent with previous reports in α-$RuCl_3$.[39] The energy-dispersive X-ray spectroscopy (EDS) and electron energy loss spectroscopy (EELS) verified that the as-exfoliated atomically-thin CrI_3 flakes were purely composed of Cr and I, with the chemical stoichiometry agreed very well with MX_3 (Figure 2e^{i} and 2f^{i}).

Indeed, the C2/m, C2/c, $P3_112$, and R$\bar{3}$ phases are unique stacking polytypes of CrI_3 arising from distinct interlayer sliding. In C2/m, C2/c, and $P3_112$ stacking registries, one unit layer is collectively translated by 1/3*a* along the zigzag directions relative to its neighboring layers. On the other hand, adjacent two layers slide relatively for $\frac{1}{\sqrt{3}}a$ along the armchair direction in the R$\overline{3}$ phase. Across from the edge few-layer regions to the interior thick domains, the 2D CrI_3 flakes may be subject to interlayer gliding to modify its stacking sequence (Figure S1).[45] Collectively, after surveying hundreds of few-layer crystals, we confirm that the C2/c (~46%) and C2/m (~41%) have much higher frequencies in the few-layer CrI_3 system as shown in the statistical counting (Figure 2k), whereas other stacking polytypes including $P3_112$ and R$\overline{3}$ only account for 13%. Therefore, the magnetic properties of few-layer CrI_3 are predominantly determined by C2/c and C2/m phases.

Magnetic properties of various stacking polytypes

To investigate the stacking order-dependent magnetic properties, we carried out first-principles DFT calculations to predict all available magnetic ground states in four different stacking registries. Our results show that the magnetic order of the C2/m, C2/c, and $P3_112$ structures is consistently AFM, while that of R$\overline{3}$ is FM (Figure 3b). These results are in good agreement with the previously reported results, that is, sliding along the zigzag direction tends to interlayer AFM coupling, while translating along the armchair direction favors FM coupling.[47] Specifically, we focused on monoclinic stackings of C2/c and C2/m, since the monoclinic stackings are ubiquitous in as-exfoliated few-layer CrI_3, and the rhombohedral stacking is rare (Figure 2k). The relative total energy difference between the magnetic configurations in C2/c and C2/m stackings, with respect to the C2/c ground state, is illustrated in Figure 3a. The magnetization directions are indicated by the black arrows. We found that the C2/c phase with AFM magnetic configuration (3 up and 3 down) is at the energy minimum (Figure S6), consistent with the experimentally observed C2/c structures with the largest proportion. Since STEM imaging is projecting a 3D crystal into a 2D plane with limited resolution perpendicular to the zone axis, we do not know the exact intralayer stacking order of a single layer MX_3, *e.g.* either *A-abc* or its reversal *A′-cba* stacking sequence (Figure S7). The uncertainty of such stacking order is a common phenomenon in 2D materials, and their consequence on interlayer magnetic interactions have not been elucidated.[22,48] To analyze the consequences of such a scenario, we constructed C2/m and C2/c inversion polytypes with inverse intralayer stacking of two iodine atomic planes at the second, fourth and sixth layers and investigated their magnetic configurations, as depicted in Figure 3b, 3c, and S8. The energy difference between inversion structures and the C2/c ground state is relatively small about 0.014 meV per formula unit (f.u.). Surprisingly, the inversion structures tend to be FM interlayer coupling, consistent with the calculation in bilayer CrI_3.[48] Besides, inversion types combined with interlayer gliding induced $R\overline{3}$ and other stacking polytypes along the armchair direction, indicate a strong FM coupling in CrI_3 thin film as observed experimentally, which are potential origins for the mysterious FM order observed in bulk CrI_3 crystals.

We now elucidate the stacking-dependent electronic structures of the C2/m and C2/c phases (Figure 3d, and S9). We note that band structures and partial density of states (PDOS) distribution of C2/m and C2/c are similar, reflecting their nearly equivalent stacking modes gliding $1/3a$ along zigzag directions if ignoring the changes of iodine atoms. For each layer, the local magnetic moment is attributed to the half-occupied t_{2g} orbital. However, the adjacent layers alternatively occupy the spin majority and spin minority t_{2g} orbital, resulting in the disappearance of the net magnetic moment. The band structures and PDOS for inversion C2/m and C2/c are plotted in Figure S10. Compared to the C2/m and C2/c phases with an AFM ground state (Figure S9), the band splitting of the inversion phases is greater due to the severe breaking of parity-time symmetry in ferromagnets. Our calculation results also show that the magnetic moments of adjacent layers in the inversion phases slightly alternate, which is different from those in the C2/m and C2/c phases with the same absolute value, reflecting the influence of different interlayer superexchanges on magnetism. In addition, from the PDOS in Figure S10, it can be seen that there are additional t_{2g} orbitals at 0.5 eV above the Fermi level, and the enhanced t_{2g}-e_g interactions favor the interlayer FM coupling.

Rich stacking polytypes in various MX_3

Rich stacking polytypes are consistently found in other layered chromium trihalides (CrX_3, X = Cl, Br, and I), as the entire family of CrX_3 possesses an identical basic-layer structure together with relatively strong (weak) in-plane (out-of-plane) exchange couplings. Since the compositions and magnetic properties of CrX_3 are different, the stacking registries in CrX_3 are diverse and highly variable. Experimentally, only two stacking orders, *i.e.*, C2/m (Figure 4a, 4c) and $R\bar{3}$ (Figure 4b, 4d), exist in few-layer $CrBr_3$. The elementary composition was verified by EDS and EELS (Figure 4e, 4f). Our atomic-resolution ADF-STEM imaging confirms that the proportion of rhombohedral stacking in the $CrBr_3$ samples is more than 80% (Figure 4g), consistent with previous observations[29]. Regardless of the stacking orders, both C2/m and $R\bar{3}$ phases in the $CrBr_3$ illustrate FM interlayer coupling as suggested by the theory (Figure 4h).

In fact, C2/c (Figure 5a, 5d), C2/m (Figure 5b, 5e), and $P3_112$ (Figure 5c, 5f) polytypes showing different interlayer couplings (Figure 5j) also exist widely in $CrCl_3$, but are different from those in CrI_3. For instance, the same C2/c structure type with six atomic layers per unit cell only accounts for 18% (Figure 5i). As expected, the $CrCl_3$ prefers C2/m stacking with a percentage of 55% (Figure 5i), reconfirming the hypothesis of C2/m enhanced AFM interlayer exchange in few-layer

$CrCl_3$,[37] consistent with our calculation results (Figure 5j). The elementary composition of the $CrCl_3$ sample was verified by EDS and EELS (Figure 5g, 5h).

Besides, multiple structure types have also been assigned to the layered α-$RuCl_3$, whose elementary composition was confirmed by EDS and EELS (Figure 6g, 6h). Consistently, we found 11% C2/c stacking polytypes in few-layer α-$RuCl_3$ crystals (Figure 6a, 6d). As shown in Figure 6, C2/m (Figure 6b, 6e) and $P3_112$ (Figure 6c, 6f) polytypes are also present in α-$RuCl_3$ with a percentage of 14% and 37%, respectively. The results are similar to $CrCl_3$ but with a preferred ferromagnetic $P3_112$ stacking (Figure 6i, 6j), reported recently in the α-$RuCl_3$ thin film.[39] Because of the relatively smaller Z atomic number of Cl (Z = 17) atoms compared to Ru (Z = 44) atoms, the signature striped topologies in the C2/c and C2/m phases are more pronounced compared to that in CrI_3. Based on our DFT results, C2/m and C2/c phases adopt AFM interlayer exchange couplings except in $CrBr_3$, which is always FM regardless of stacking orders, as shown in Table 1. However, $P3_112$ and $R\bar{3}$ stackings exhibit completely different magnetic properties in MX_3 (Figure 3b, 5j, and 6j). Surprisingly, C2/c and C2/m inversion structures in $CrCl_3$ and $RuCl_3$ tend to be FM and ferrimagnetic (FerriM) interlayer coupling, respectively.

Interestingly, regardless of the MX_3 crystals produced by chemical vapor transport (CVT) or purchased from commercial products, $CrBr_3$ is almost pure $R\bar{3}$ phase, mixed phases often occur in $CrCl_3$, whereas other novel structures existing in all the MX_3 are waiting for exploration especially in α-$RuCl_3$, as depicted in Figure S11. Furthermore, metal nanoparticles are observed by electron beam reduction from Ru (III) ions, similar to previous observation.[39]

Our atomic-scale STEM results provide direct evidence that various stacking polytypes can exist in few-layer MX_3 flakes. The distinct magnetic ground states of MX_3 polytypes demonstrate an effective way to modulate the 2D magnetism via changing the stacking sequences.[6] For instance, the AFM interlayer exchange in CrI_3 is broken by changing the stacking sequence to FM C2/c- and C2/m-inversion symmetry. The multiple structures provide insights into understanding different ground states in ultrathin CrI_3 films, which also give clues for the mystery of phase transitions. The internal strain and multiple phases may suppress the C2/m to $R\bar{3}$ (AFM to FM) transformation when the layer number of MX_3 is reduced to atomically thin.

Strain soliton boundaries induced phase transition

When one stacking polytype translates into another, this is usually accompanies by a strain soliton boundary, which creates non-trivial magnetic or electronic states,[49,50] as shown in Figure 7. It can be clearly seen that the stacking order transition from the rhombohedral (R) sequence (upper region) to the monoclinic (M) sequence (lower region), is gradually accommodated by strain soliton boundaries (Figure 7b). The layer stacking in the R phase is illustrated by periodic dark spots arrangement while that in the M sequence is the signature stripy topology (Figure 7b). Toward the top and bottom sides of the STEM image (Figure 7c), the periodic bright spot arrangement represents the stacked C2/m and $R\bar{3}$ crystals. The brightness decreases at the center of the boundary, and the hexagonal patterns evolve into linear features along the $(33\bar{1})$ plane of the C2/m structure (Figure 7c). Thus, the symmetry is broken as the stacking changes across the boundary, which is always accompanied by the formation of large strain gradients (Figure S12). However, the measurement of $(33\bar{1})$ interplane distance at the boundary region shows no change compared to that of the R and M phase (Figure 7c), indicating that the transition from R to M can be achieved solely through the shear force along the $(33\bar{1})$ plane. The high-density dislocations in MX_3 suggest that the stacking transition is likely intrinsic, which is universal to vdW materials with weak interlayer coupling, resulting in the local interlayer gliding on one side of the boundary and the creation of discrete stacking domains (Figure S1).[51]

A schematic of stacking across the R/M boundary exhibiting shear and tensile strain is shown in Figure 7a. Based on our observations, we present the following picture to describe the magnetic configurations in CrI_3 flakes, as illustrated in Figure 7d, describing the coupling of the magnetic response to the stacking order. It is known that the magnetic ground state of few-layer CrI_3 is highly dependent on the stacking order[26,31] and strain.[47] Therefore, this observation provides the opportunity to unveil the complexities of the magnetism of this compound where a structural phase fails to be captured. For instance, the gap between AFM coupling in monoclinic (C2/c and C2/m) thin layers and FM bulk with a rhombohedral stacking ($R\bar{3}$) can be compensated by increasing the proportion of the R sequence. We found that few-layer MX_3 materials are composed of a mixture of R and M phases, which may be retained at a low temperature since no phase transition happens during the cooling in few-layer MX_3[30,37] and the M phase can coexist with the R phase down to low temperature in the bulk.[52] In light of our findings, it is not surprising that diverse magnetic orders can coexist in the same flake because each can have different amounts of various types pf stacking order.

CONCLUSION

In summary, we demonstrated a robust dry-transfer method to transfer air-sensitive few-layer MX_3 layers for atomic-resolution electron microscopy study. We systematically analyzed the polytypes in a library of MX_3, which provides a comprehensive picture of the magnetism in MX_3 and points to the possibility of engineering magnetic heterostructures and textures within the same material by interlayer vdW coupling. Our observations illustrate that the monoclinic stackings (C2/c and

C2/m) are predominant in several few-layer MX_3 and are responsible for the 2D magnetism. The reversed structure of C2/c and C2/m together with a high density of strain soliton boundaries contribute to the FM order in few-layer MX_3. These results provide useful insights into the complex magnetic behavior in atomically thin CrI_3, and also clues to designing magnetic phases and developing new functionalities in 2D magnets via stacking engineering.

Experimental Section

Sample preparation. The atomically-thin MX_3 flakes were exfoliated from bulk crystals produced by the CVT method[8] or from the commercial products (CrI_3 and $CrBr_3$ are commercial products, $RuCl_3$ and $CrCl_3$ are from both), and then transferred to the STEM substrate (Cu Quantifoil grid) by dry transfer technique for STEM observation. Specially, the atomically-thin MX_3 flakes were exfoliated on PDMS stamps, contacted MX_3 flakes with the target STEM substrate, and then peeled the PDMS from the substrate by mild heating. During this transfer process, no chemical etchants nor water are applied. Low-magnification STEM image (Figure S1), EDS, and EELS verified that the as-exfoliated atomically-thin MX_3 flakes were composed of M and X, with the chemical stoichiometry agreeing very well with MX_3 (Figure 2i-j, 4e-f, 5g-h, 6g-h).

ADF-STEM imaging, processing, and simulation. Atomic-resolution ADF-STEM imaging was performed on an aberration-corrected Nion U-HERMES200 microscope, equipped with a cold field-emission gun operating at 60 kV. The convergence semiangle of the probe was around 35 mrad. Image simulations were performed with the Prismatic package assuming an aberration-free probe with a probe size of approximately 1 Å. The convergence semiangle and accelerating voltage were in line with the experiments. The collection angle for ADF imaging was between 80 and 200 mrad. ADF-STEM images were filtered by Gaussian filters, and the positions of atomic columns were located by finding the local maxima of the filtered series. The EDS and EELS were collected and processed in JEOL ARM200F at 80 kV.

DFT calculations. Our first-principles calculations were based on density functional theory (DFT) as implemented in the Vienna *Ab initio* Simulation Package (VASP),[53] using the projector augmented-wave method.[54] The generalized gradient approximation (GGA) with the Perdew-Burke-Ernzerhof[55] realization was adopted for the exchange-correlation functional. We set the on-site effective Hubbard interaction U= 4 eV (2 eV) in considering the electron correlation of 3*d* (4*d*) electrons of Cr (Ru) atoms. The plane-wave cutoff energy was set to 450 eV. A Monkhorst-Pack k-point mesh[56] with a size of 9×9×2 was used for the Brillouin zone sampling. The crystal structure was optimized until the forces on the ions were less than 0.01 eV/Å, and the total energy was converged to 10^{-5} eV with the Gaussian smearing method. The zero-damping DFT-D3 method was adopted to describe the interlayer van der Waals interaction.

ASSOCIATED CONTENT

Supporting information

The supporting information is available free of charge at

Discussion on the geometrical and electronic structure differences between various stacking polytypes of MX_3.

AUTHOR INFORMATION

Corresponding Authors

Kian Ping Loh -*Department of Applied Pjysics, Hong Kong Polytechnic University, Hung Hom, Hong Kong SAR;* Email: kploh@polyu.edu.hk

Xiaoxu Zhao - *School of Materials Science and Engineering, Peking University, Beijing 100871, China*; Email: xiaoxuzhao@pku.edu.cn

Authors

Xiaocang Han- *School of Materials Science and Engineering, Peking University, Beijing 100871, China*

Jing-Yang You - *Department of Physics, National University of Singapore, 2 Science Drive 3, 117551, Singapore*

Shengqiang Wu - *School of Materials Science and Engineering, Peking University, Beijing 100871, China*

Runlai Li - *College of Polymer Science & Engineering, State Key Laboratory of Polymer Materials Engineering, Sichuan University, Chengdu, 610065, China*

Yuan Ping Feng - *Department of Physics, National University of Singapore, 2 Science Drive 3, 117551, Singapore*

Complete contact information is available at:

Author Contributions

‖X. H., & J. Y., contributed equally to this work. X. Z., and K. P. L. conceived the idea and supervised the execution of the experimental work. X. H., X. Z., and S. W. performed the electron microscopy experiments and data analysis. J. Y. did DFT calculations and theoretical analysis under the supervision of Y. P. F. and R. L. conducted sample preparations. X. H. and S. W. did the image simulation.

Notes

The authors declare no competing financial interest

ACKNOWLEDGEMENTS

X.X.Z.thank the Peking University startup funding, and the National Natural Science Foundation of China (grant no.52273279). J.Y.Y and Y.P.F. are supported by the Ministry of Education, Singapore, under its MOE AcRF Tier 3 Award MOE2018-T3-1-002. K. P. Loh acknowledges Grant P0043063 and Global STEM professorship of Hong Kong Polytechnic University.

REFERENCES

(1) Gong, C.; Li, L.; Li, Z.; Ji, H.; Stern, A.; Xia, Y.; Cao, T.; Bao, W.; Wang, C.; Wang, Y.; Qiu, Z. Q.; Cava, R. J.; Louie, S. G.; Xia, J.; Zhang, X. Discovery of Intrinsic Ferromagnetism in Two-Dimensional van Der Waals Crystals. *Nature* **2017**, *546* (7657), 265–269. https://doi.org/10.1038/nature22060.

(2) Huang, B.; Clark, G.; Navarro-Moratalla, E.; Klein, D. R.; Cheng, R.; Seyler, K. L.; Zhong, Di.; Schmidgall, E.; McGuire, M. A.; Cobden, D. H.; Yao, W.; Xiao, D.; Jarillo-Herrero, P.; Xu, X. Layer-Dependent Ferromagnetism in a van Der Waals Crystal down to the Monolayer Limit. *Nature* **2017**, *546* (7657), 270–273. https://doi.org/10.1038/nature22391.

(3) Gibertini, M.; Koperski, M.; Morpurgo, A. F.; Novoselov, K. S. Magnetic 2D Materials and Heterostructures. *Nat. Nanotechnol.* **2019**, *14* (5), 408–419. https://doi.org/10.1038/s41565-019-0438-6.

(4) Gong, C.; Zhang, X. Two-Dimensional Magnetic Crystals and Emergent Heterostructure Devices. *Science (80-.).* **2019**, *363* (6428). https://doi.org/10.1126/science.aav4450.

(5) Lei, C.; Chittari, B. L.; Nomura, K.; Banerjee, N.; Jung, J.; Macdonald, A. H. Magnetoelectric Response of Antiferromagnetic CrI3 Bilayers. *Nano Lett.* **2021**, *21* (5), 1948–1954. https://doi.org/10.1021/acs.nanolett.0c04242.

(6) Soriano, D.; Katsnelson, M. I.; Fernández-Rossier, J. Magnetic Two-Dimensional Chromium Trihalides: A Theoretical Perspective. *Nano Lett.* **2020**, *20* (9), 6225–6234. https://doi.org/10.1021/acs.nanolett.0c02381.

(7) Song, T.; Cai, X.; Tu, M. W. Y.; Zhang, X.; Huang, B.; Wilson, N. P.; Seyler, K. L.; Zhu, L.; Taniguchi, T.; Watanabe, K.; McGuire, M. A.; Cobden, D. H.; Xiao, D.; Yao, W.; Xu, X. Giant Tunneling Magnetoresistance in Spin-Filter van Der Waals Heterostructures. *Science (80-.).* **2018**, *360* (6394), 1214–1218. https://doi.org/10.1126/science.aar4851.

(8) Wang, Z.; Gutiérrez-Lezama, I.; Ubrig, N.; Kroner, M.; Gibertini, M.; Taniguchi, T.; Watanabe, K.; Imamoğlu, A.; Giannini, E.; Morpurgo, A. F. Very Large Tunneling Magnetoresistance in Layered Magnetic Semiconductor CrI3. *Nat. Commun.* **2018**, *9*, 2516. https://doi.org/10.1038/s41467-018-04953-8.

(9) Banerjee, A.; Yan, J.; Knolle, J.; Bridges, C. A.; Stone, M. B.; Lumsden, M. D.; Mandrus, D. G.; Tennant, D. A.; Moessner, R.; Nagler, S. E. Neutron Scattering in the Proximate Quantum Spin Liquid α-RuCl3. *Science (80-.).* **2017**, *356* (6342), 1055–1059. https://doi.org/10.1126/science.aah6015.

(10) Banerjee, A.; Bridges, C. A.; Yan, J. Q.; Aczel, A. A.; Li, L.; Stone, M. B.; Granroth, G. E.; Lumsden, M. D.; Yiu, Y.; Knolle, J.; Bhattacharjee, S.; Kovrizhin, D. L.; Moessner, R.; Tennant, D. A.; Mandrus, D. G.; Nagler, S. E. Proximate Kitaev Quantum Spin Liquid Behaviour in a Honeycomb Magnet. *Nat. Mater.* **2016**, *15* (7), 733–740. https://doi.org/10.1038/nmat4604.

(11) Chen, L.; Chung, J. H.; Gao, B.; Chen, T.; Stone, M. B.; Kolesnikov, A. I.; Huang, Q.; Dai, P. Topological Spin Excitations in Honeycomb Ferromagnet CrI3. *Phys. Rev. X* **2018**, *8* (4), 41028. https://doi.org/10.1103/PhysRevX.8.041028.

(12) Lee, I.; Utermohlen, F. G.; Weber, D.; Hwang, K.; Zhang, C.; Van Tol, J.; Goldberger, J. E.; Trivedi, N.; Hammel, P. C. Fundamental Spin Interactions Underlying the Magnetic

Anisotropy in the Kitaev Ferromagnet CrI3. *Phys. Rev. Lett.* **2020**, *124* (1), 17201. https://doi.org/10.1103/PhysRevLett.124.017201.

(13) Wu, J.; Yao, Y.; Lin, M. L.; Rösner, M.; Du, Z.; Watanabe, K.; Taniguchi, T.; Tan, P. H.; Haas, S.; Wang, H. Spin–Phonon Coupling in Ferromagnetic Monolayer Chromium Tribromide. *Adv. Mater.* **2022**, *34* (20), 1–8. https://doi.org/10.1002/adma.202108506.

(14) Klein, D. R.; MacNeill, D.; Lado, J. L.; Soriano, D.; Navarro-Moratalla, E.; Watanabe, K.; Taniguchi, T.; Manni, S.; Canfield, P.; Fernández-Rossier, J.; Jarillo-Herrero, P. Probing Magnetism in 2D van Der Waals Crystalline Insulators via Electron Tunneling. *Science (80-.).* **2018**, *360* (6394), 1218–1222. https://doi.org/10.1126/science.aar3617.

(15) Kim, H. H.; Yang, B.; Li, S.; Jiang, S.; Jin, C.; Tao, Z.; Nichols, G.; Sfigakis, F.; Zhong, S.; Li, C.; Tian, S.; Cory, D. G.; Miao, G. X.; Shan, J.; Mak, K. F.; Lei, H.; Sun, K.; Zhao, L.; Tsen, A. W. Evolution of Interlayer and Intralayer Magnetism in Three Atomically Thin Chromium Trihalides. *Proc. Natl. Acad. Sci. U. S. A.* **2019**, *166* (23), 11131–11136. https://doi.org/10.1073/pnas.1902100116.

(16) Jiang, S.; Li, L.; Wang, Z.; Shan, J.; Mak, K. F. Spin Tunnel Field-Effect Transistors Based on Two-Dimensional van Der Waals Heterostructures. *Nat. Electron.* **2019**, *2* (4), 159–163. https://doi.org/10.1038/s41928-019-0232-3.

(17) Cardoso, C.; Soriano, D.; García-Martínez, N. A.; Fernández-Rossier, J. Van Der Waals Spin Valves. *Phys. Rev. Lett.* **2018**, *121* (6), 67701. https://doi.org/10.1103/PhysRevLett.121.067701.

(18) Cenker, J.; Huang, B.; Suri, N.; Thijssen, P.; Miller, A.; Song, T.; Taniguchi, T.; Watanabe, K.; McGuire, M. A.; Xiao, D.; Xu, X. Direct Observation of Two-Dimensional

Magnons in Atomically Thin CrI3. *Nat. Phys.* **2021**, *17* (1), 20–25. https://doi.org/10.1038/s41567-020-0999-1.

(19) Huang, B.; Clark, G.; Klein, D. R.; MacNeill, D.; Navarro-Moratalla, E.; Seyler, K. L.; Wilson, N.; McGuire, M. A.; Cobden, D. H.; Xiao, D.; Yao, W.; Jarillo-Herrero, P.; Xu, X. Electrical Control of 2D Magnetism in Bilayer CrI3. *Nat. Nanotechnol.* **2018**, *13* (7), 544–548. https://doi.org/10.1038/s41565-018-0121-3.

(20) Song, T.; Fei, Z.; Yankowitz, M.; Lin, Z.; Jiang, Q.; Hwangbo, K.; Zhang, Q.; Sun, B.; Taniguchi, T.; Watanabe, K.; McGuire, M. A.; Graf, D.; Cao, T.; Chu, J. H.; Cobden, D. H.; Dean, C. R.; Xiao, D.; Xu, X. Switching 2D Magnetic States via Pressure Tuning of Layer Stacking. *Nat. Mater.* **2019**, *18* (12), 1298–1302. https://doi.org/10.1038/s41563-019-0505-2.

(21) Jiang, S.; Li, L.; Wang, Z.; Mak, K. F.; Shan, J. Controlling Magnetism in 2D CrI3 by Electrostatic Doping. *Nat. Nanotechnol.* **2018**, *13* (7), 549–553. https://doi.org/10.1038/s41565-018-0135-x.

(22) Chen, W.; Sun, Z.; Wang, Z.; Gu, L.; Xu, X.; Wu, S.; Gao, C. Direct Observation of van Der Waals Stacking–Dependent Interlayer Magnetism. *Science (80-.).* **2019**, *366* (6468), 983–987. https://doi.org/10.1126/science.aav1937.

(23) McGuire, M. A.; Dixit, H.; Cooper, V. R.; Sales, B. C. Coupling of Crystal Structure and Magnetism in the Layered, Ferromagnetic Insulator CrI3. *Chem. Mater.* **2015**, *27* (2), 612–620. https://doi.org/10.1021/cm504242t.

(24) Xie, H.; Luo, X.; Ye, G.; Ye, Z.; Ge, H.; Sung, S. H.; Rennich, E.; Yan, S.; Fu, Y.; Tian, S.; Lei, H.; Hovden, R.; Sun, K.; He, R.; Zhao, L. Twist Engineering of the Two-

Dimensional Magnetism in Double Bilayer Chromium Triiodide Homostructures. *Nat. Phys.* **2022**, *18* (1), 30–36. https://doi.org/10.1038/s41567-021-01408-8.

(25) Song, T.; Sun, Q. C.; Anderson, E.; Wang, C.; Qian, J.; Taniguchi, T.; Watanabe, K.; McGuire, M. A.; Stöhr, R.; Xiao, D.; Cao, T.; Wrachtrup, J.; Xu, X. Direct Visualization of Magnetic Domains and Moiré Magnetism in Twisted 2D Magnets. *Science (80-.).* **2021**, *374* (6571), 1140–1144. https://doi.org/10.1126/science.abj7478.

(26) Sivadas, N.; Okamoto, S.; Xu, X.; Fennie, C. J.; Xiao, D. Stacking-Dependent Magnetism in Bilayer CrI 3. *Nano Lett.* **2018**, *18* (12), 7658–7664. https://doi.org/10.1021/acs.nanolett.8b03321.

(27) Jiang, P.; Wang, C.; Chen, D.; Zhong, Z.; Yuan, Z.; Lu, Z. Y.; Ji, W. Stacking Tunable Interlayer Magnetism in Bilayer CrI3. *Phys. Rev. B* **2019**, *99* (14), 144401. https://doi.org/10.1103/PhysRevB.99.144401.

(28) Sun, Z.; Yi, Y.; Song, T.; Clark, G.; Huang, B.; Shan, Y.; Wu, S.; Huang, D.; Gao, C.; Chen, Z.; McGuire, M.; Cao, T.; Xiao, D.; Liu, W. T.; Yao, W.; Xu, X.; Wu, S. Giant Nonreciprocal Second-Harmonic Generation from Antiferromagnetic Bilayer CrI3. *Nature* **2019**, *572* (7770), 497–501. https://doi.org/10.1038/s41586-019-1445-3.

(29) Hamer, M. J.; Hopkinson, D. G.; Clark, N.; Zhou, M.; Wang, W.; Zou, Y.; Kelly, D. J.; Bointon, T. H.; Haigh, S. J.; Gorbachev, R. V. Atomic Resolution Imaging of CrBr3 Using Adhesion-Enhanced Grids. *Nano Lett.* **2020**, *20* (9), 6582–6589. https://doi.org/10.1021/acs.nanolett.0c02346.

(30) Ray, A.; Shao, Y.-T.; Xu, Y.; Sivadas, N.; Li, T.; Wang, Z.; Mak, K. F.; Shan, J.; Fennie, C.; Muller, D. Mapping Stacking and Stacking Defects in the 2D Ferromagnet CrI3.

Microsc. Microanal. **2020**, *26* (S2), 636–638. https://doi.org/10.1017/s1431927620015366.

(31) Thiel, L.; Wang, Z.; Tschudin, M. A.; Rohner, D.; Gutiérrez-Lezama, I.; Ubrig, N.; Gibertini, M.; Giannini, E.; Morpurgo, A. F.; Maletinsky, P. Probing Magnetism in 2D Materials at the Nanoscale with Single-Spin Microscopy. *Science (80-.).* **2019**, *364* (6444), 973–976. https://doi.org/10.1126/science.aav6926.

(32) Soriano, D.; Cardoso, C.; Fernández-Rossier, J. Interplay between Interlayer Exchange and Stacking in CrI3 Bilayers. *Solid State Commun.* **2019**, *299* (May), 113662. https://doi.org/10.1016/j.ssc.2019.113662.

(33) Jang, S. W.; Jeong, M. Y.; Yoon, H.; Ryee, S.; Han, M. J. Microscopic Understanding of Magnetic Interactions in Bilayer CrI3. *Phys. Rev. Mater.* **2019**, *3* (3), 1–6. https://doi.org/10.1103/PhysRevMaterials.3.031001.

(34) Tsubokawa, I. On the Magnetic Properties of a CrBr3 Single Crystal. *J. Phys. Soc. Japan* **1960**, *15* (9), 1664–1668. https://doi.org/10.1143/JPSJ.15.1664.

(35) Cable, J. W.; Wilkinson, M. K.; Wollan, E. O. Neutron Diffraction Investigation of Antiferromagnetism in CrCl3. *J. Phys. Chem. Solids* **1961**, *19* (1), 29–34. https://doi.org/https://doi.org/10.1016/0022-3697(61)90053-1.

(36) Morosin, B.; Narath, A. X-Ray Diffraction and Nuclear Quadrupole Resonance Studies of Chromium Trichloride. *J. Chem. Phys.* **1964**, *40* (7), 1958–1967. https://doi.org/10.1063/1.1725428.

(37) Klein, D. R.; MacNeill, D.; Song, Q.; Larson, D. T.; Fang, S.; Xu, M.; Ribeiro, R. A.; Canfield, P. C.; Kaxiras, E.; Comin, R.; Jarillo-Herrero, P. Enhancement of Interlayer Exchange in an Ultrathin Two-Dimensional Magnet. *Nat. Phys.* **2019**, *15* (12), 1255–1260. https://doi.org/10.1038/s41567-019-0651-0.

(38) Cao, H. B.; Banerjee, A.; Yan, J. Q.; Bridges, C. A.; Lumsden, M. D.; Mandrus, D. G.; Tennant, D. A.; Chakoumakos, B. C.; Nagler, S. E. Low-Temperature Crystal and Magnetic Structure of α-RuCl3. *Phys. Rev. B* **2016**, *93* (13), 1–8. https://doi.org/10.1103/PhysRevB.93.134423.

(39) Ziatdinov, M.; Banerjee, A.; Maksov, A.; Berlijn, T.; Zhou, W.; Cao, H. B.; Yan, J. Q.; Bridges, C. A.; Mandrus, D. G.; Nagler, S. E.; Baddorf, A. P.; Kalinin, S. V. Atomic-Scale Observation of Structural and Electronic Orders in the Layered Compound α-RuCl3. *Nat. Commun.* **2016**, *7*, 13774. https://doi.org/10.1038/ncomms13774.

(40) Kim, H. S.; Kee, H. Y. Crystal Structure and Magnetism in α-RuCl3: An Ab Initio Study. *Phys. Rev. B* **2016**, *93* (15), 1–10. https://doi.org/10.1103/PhysRevB.93.155143.

(41) Shcherbakov, D.; Stepanov, P.; Weber, D.; Wang, Y.; Hu, J.; Zhu, Y.; Watanabe, K.; Taniguchi, T.; Mao, Z.; Windl, W.; Goldberger, J.; Bockrath, M.; Lau, C. N. Raman Spectroscopy, Photocatalytic Degradation, and Stabilization of Atomically Thin Chromium Tri-Iodide. *Nano Lett.* **2018**, *18* (7), 4214–4219. https://doi.org/10.1021/acs.nanolett.8b01131.

(42) Castellanos-Gomez, A.; Buscema, M.; Molenaar, R.; Singh, V.; Janssen, L.; Van Der Zant, H. S. J.; Steele, G. A. Deterministic Transfer of Two-Dimensional Materials by All-

Dry Viscoelastic Stamping. *2D Mater.* **2014**, *1* (1). https://doi.org/10.1088/2053-1583/1/1/011002.

(43) Hartel, P.; Rose, H.; Dinges, C. Conditions and Reasons for Incoherent Imaging in STEM. *Ultramicroscopy* **1996**, *63* (2), 93–114. https://doi.org/10.1016/0304-3991(96)00020-4.

(44) Krivanek, O. L.; Chisholm, M. F.; Nicolosi, V.; Pennycook, T. J.; Corbin, G. J.; Dellby, N.; Murfitt, M. F.; Own, C. S.; Szilagyi, Z. S.; Oxley, M. P.; Pantelides, S. T.; Pennycook, S. J. Atom-by-Atom Structural and Chemical Analysis by Annular Dark-Field Electron Microscopy. *Nature* **2010**, *464* (7288), 571–574. https://doi.org/10.1038/nature08879.

(45) Wang, F.; Zhang, Z.; Zhang, Y.; Nie, A.; Zhao, W.; Wang, D.; Huang, F.; Zhai, T. Honeycomb RhI3 Flakes with High Environmental Stability for Optoelectronics. *Adv. Mater.* **2020**, *32* (25). https://doi.org/10.1002/adma.202001979.

(46) Cenker, J.; Sivakumar, S.; Xie, K.; Miller, A.; Thijssen, P.; Liu, Z.; Dismukes, A.; Fonseca, J.; Anderson, E.; Zhu, X.; Roy, X.; Xiao, D.; Chu, J. H.; Cao, T.; Xu, X. Reversible Strain-Induced Magnetic Phase Transition in a van Der Waals Magnet. *Nat. Nanotechnol.* **2022**, *17* (3), 256–261. https://doi.org/10.1038/s41565-021-01052-6.

(47) Zhang, Z.; You, J. Y.; Gu, B.; Su, G. Emergent Magnetic States Due to Stacking and Strain in the van Der Waals Magnetic Trilayer CrI3. *Phys. Rev. B* **2021**, *104* (17), 1–8. https://doi.org/10.1103/PhysRevB.104.174433.

(48) Kong, X.; Yoon, H.; Han, M. J.; Liang, L. Switching Interlayer Magnetic Order in Bilayer CrI3 by Stacking Reversal. *Nanoscale* **2021**, *13* (38), 16172–16181. https://doi.org/10.1039/d1nr02480a.

(49) Xu, Y.; Ray, A.; Shao, Y. T.; Jiang, S.; Lee, K.; Weber, D.; Goldberger, J. E.; Watanabe, K.; Taniguchi, T.; Muller, D. A.; Mak, K. F.; Shan, J. Coexisting Ferromagnetic–Antiferromagnetic State in Twisted Bilayer CrI3. *Nat. Nanotechnol.* **2022**, *17* (2), 143–147. https://doi.org/10.1038/s41565-021-01014-y.

(50) Hejazi, K.; Luo, Z. X.; Balents, L. Noncollinear Phases in Moiré Magnets. *Proc. Natl. Acad. Sci. U. S. A.* **2020**, *117* (20), 10721–10726. https://doi.org/10.1073/pnas.2000347117.

(51) Lin, J.; Fang, W.; Zhou, W.; Lupini, A. R.; Idrobo, J. C.; Kong, J.; Pennycook, S. J.; Pantelides, S. T. AC/AB Stacking Boundaries in Bilayer Graphene. *Nano Lett.* **2013**, *13* (7), 3262–3268. https://doi.org/10.1021/nl4013979.

(52) Meseguer-Sánchez, J.; Popescu, C.; García-Muñoz, J. L.; Luetkens, H.; Taniashvili, G.; Navarro-Moratalla, E.; Guguchia, Z.; Santos, E. J. G. Coexistence of Structural and Magnetic Phases in van Der Waals Magnet CrI3. *Nat. Commun.* **2021**, *12* (1), 6265. https://doi.org/10.1038/s41467-021-26342-4.

(53) Kresse, G.; Furthmüller, J. Efficient Iterative Schemes for Ab Initio Total-Energy Calculations Using a Plane-Wave Basis Set. *Phys. Rev. B - Condens. Matter Mater. Phys.* **1996**, *54* (16), 11169–11186. https://doi.org/10.1103/PhysRevB.54.11169.

(54) Blöchl, P. E. Projector Augmented-Wave Method. *Phys. Rev. B* **1994**, *50* (24), 17953–17979. https://doi.org/10.1103/PhysRevB.50.17953.

(55) Perdew, J. P.; Burke, K.; Ernzerhof, M. Generalized Gradient Approximation Made Simple. *Phys. Rev. Lett.* **1996**, *77* (18), 3865–3868. https://doi.org/10.1103/PhysRevLett.77.3865.

(56) Monkhorst, H. J.; Pack, J. D. Special Points for Brillouin-Zone Integrations. *Phys. Rev. B* **1976**, *13*, 5188–5192. https://doi.org/10.1103/PhysRevB.16.1748.

Figures:

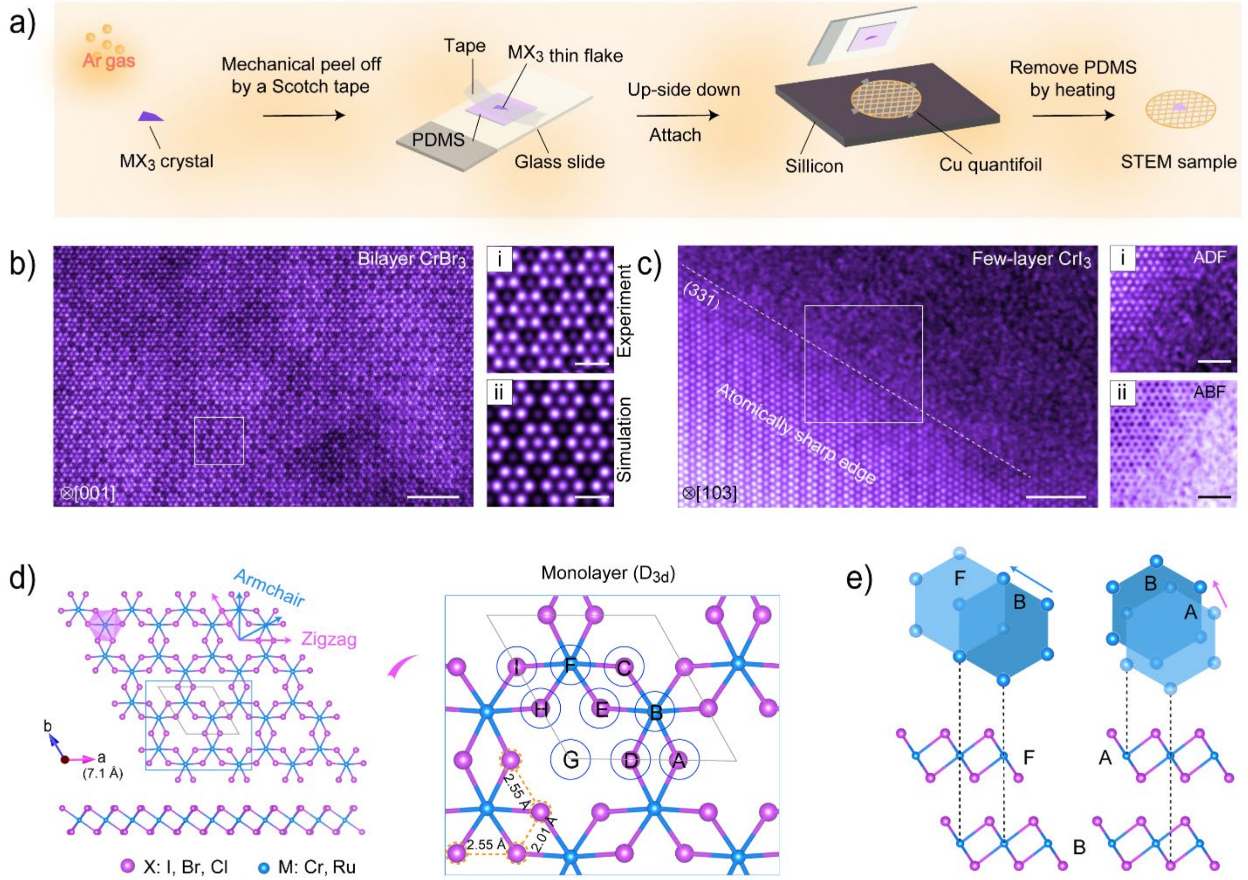

Figure 1. Dry transfer method for atomically thin MX$_3$ flakes. a) Schematic illustration of the dry transfer method. b, c) Atomic-resolution ADF-STEM images showing the success of the dry transfer method. The as-transferred bilayer CrBr$_3$ (b) was confirmed by the consistency of experimental (i) and simulated (ii) images. The as-transferred atomically-thin CrI$_3$ (c) displays a clean and atomically sharp edge in both ADF (i) and annular bright field (ABF) (ii) imaging. d) Atomic model of the DFT optimized monolayer CrI$_3$. The top and side views are depicted in the top and bottom panels. An enlarged atomic model showing 9 stacking sites for the second layer is depicted in the right panel. The armchair and zigzag directions are labeled by light cyan and purple

lines, respectively. e) Top and side views of bilayer MX_3 in *AB* [010] and *FB* [210] stackings. In the top view, iodine atoms are omitted for clarity. Scale bars: b, c, 2 nm; $b^{i,\,ii}$, 0.5 nm; $c^{i,\,ii}$, 1 nm.

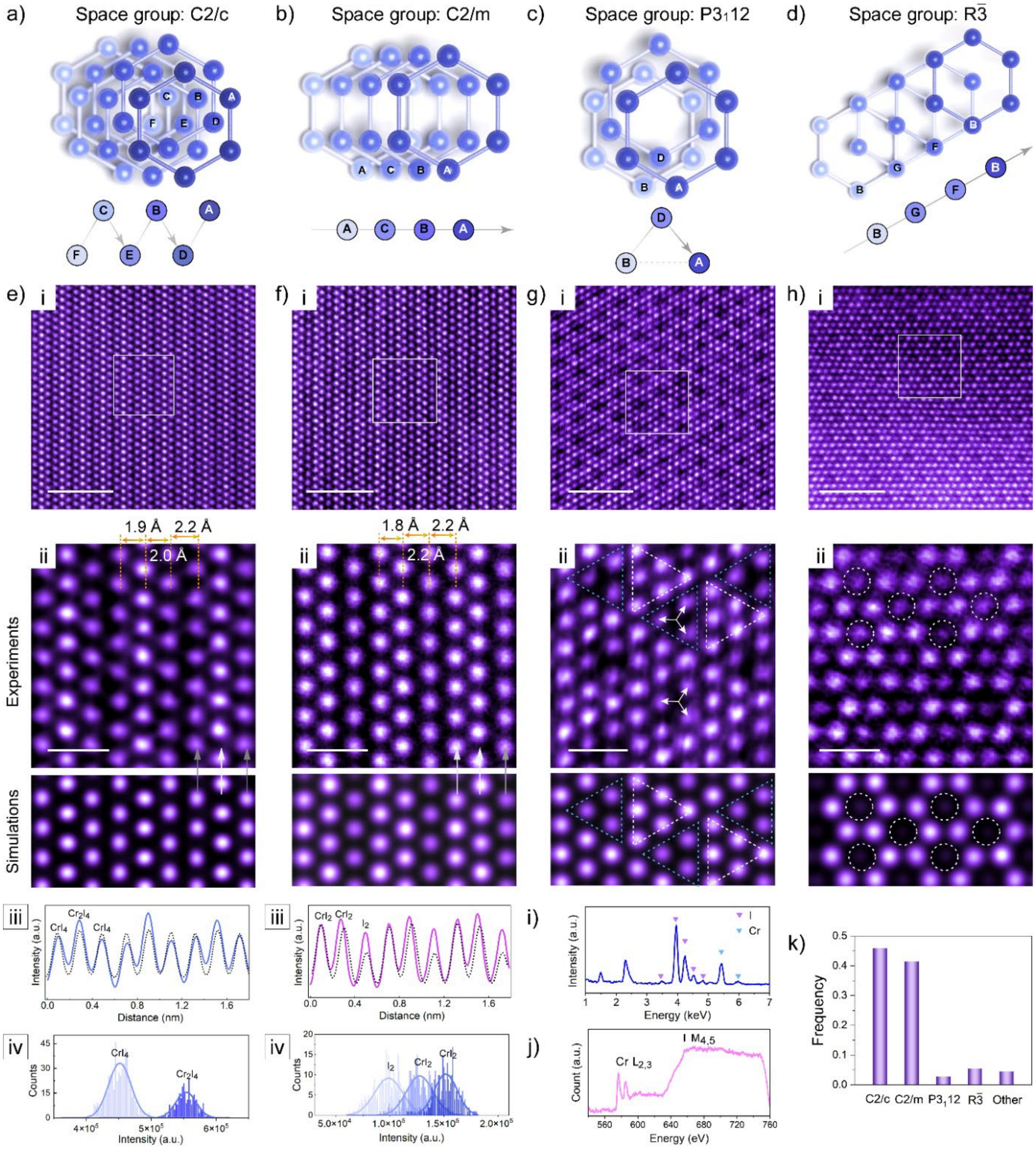

Figure 2. Atomic structures of various stacking polytypes of CrI_3. a-d) The atomic models of layered CrI_3 viewed along the *c* axis in C2/c (a), C2/m (b), $P3_112$ (c), and $R\bar{3}$ (d) phases. For clarity,

the Cr atoms in different layers are shown by different colors (I^- ions are omitted for clarity). e-h) Top (i), atomic-resolution ADF-STEM images showing different stacking polytypes of few-layer CrI_3 crystals consisting of C2/c, C2/m, $P3_112$, and $R\bar{3}$ phases from left to right, respectively; middle (ii), the zoom-in images from white regions in (i) and corresponding simulated images; bottom (iii and iv), the averaged intensity of all atomic sites (iii) and statistical analysis of intensity (iv) from experimental images of C2/c and C2/m in (e^i) and (f^i). The simulated intensity line profiles (labeled by a black dotted line) are presented for comparison. g, h) EDS and EEL spectra of core-level edges of CrI_3 thin film. k) The frequency of different stacking structures, including C2/c, C2/m, $P3_112$, and $R\bar{3}$ and other stackings, after counting 110 flakes. The white arrows indicated the displacement of iodine columns in (g^{ii}). Scale bars: $(e\text{-}h)^i$, 2 nm; $(e\text{-}h)^{ii}$, 0.5 nm.

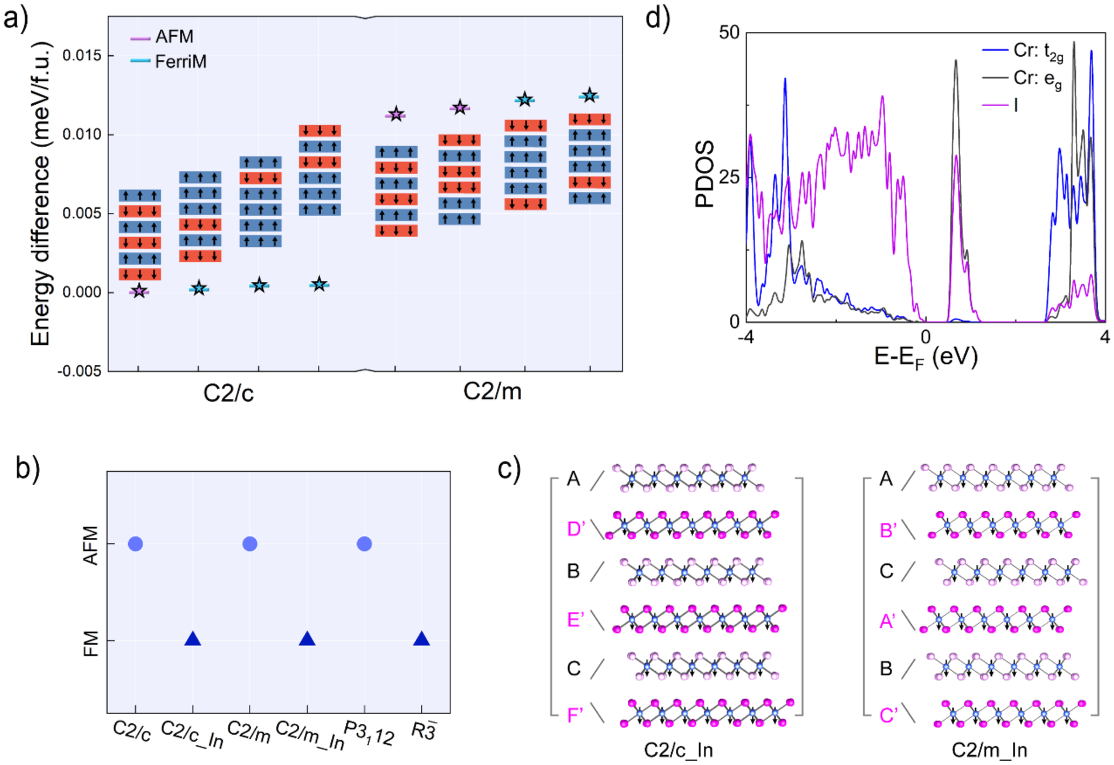

Figure 3. Electronic structures of various stacking polytypes of CrI_3. a) The relative total energy of the C2/c and C2/m structure with different magnetic configurations, with respect to the C2/c ground state. The magnetization directions along the *c* axis are indicated by black arrows with blue (spin up) and red background (spin down). b) The calculated magnetic ground state of different stacking polytypes. c) The side view of inversion structures of C2/c and C2/m, denoted as C2/c_In and C2/m_In. Inversion stacking arrangements are created by switching the two iodine atomic layers upside down in one sandwich unit cell (intralayer polymorph). d) The corresponding PDOS for the ground state of C2/c. The PDOS of each orbital channel is represented by different colors as denoted in (d).

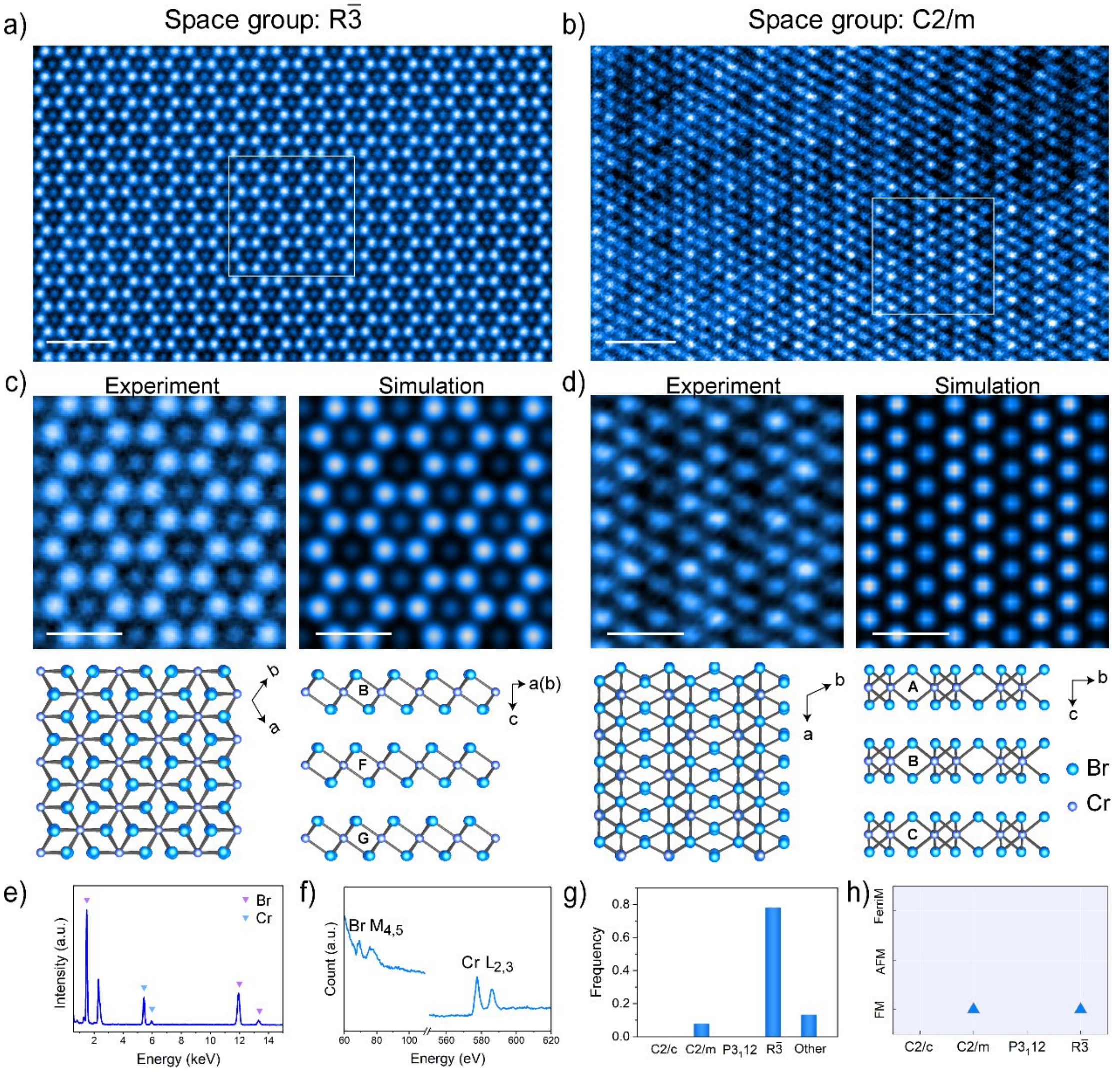

Figure 4. Atomic structures of various stacking polytypes of $CrBr_3$ a, b) Atomic-resolution ADF-STEM images showing the R$\overline{3}$ (a) and C2/m (b) stacking polytypes in few-layer $CrBr_3$ crystals. c, d) Left, enlarged STEM images corresponding to the regions highlighted with white boxes in (a, b), respectively; right, the corresponding simulated images; e, f) EDS (e) and EEL (f) spectra of core-level edges of $CrBr_3$ thin film. g, h) The frequency (g) and calculated magnetic ground state (h) of different stacking polytypes. Scale bars: a, b, 2 nm; c, d, 0.5 nm.

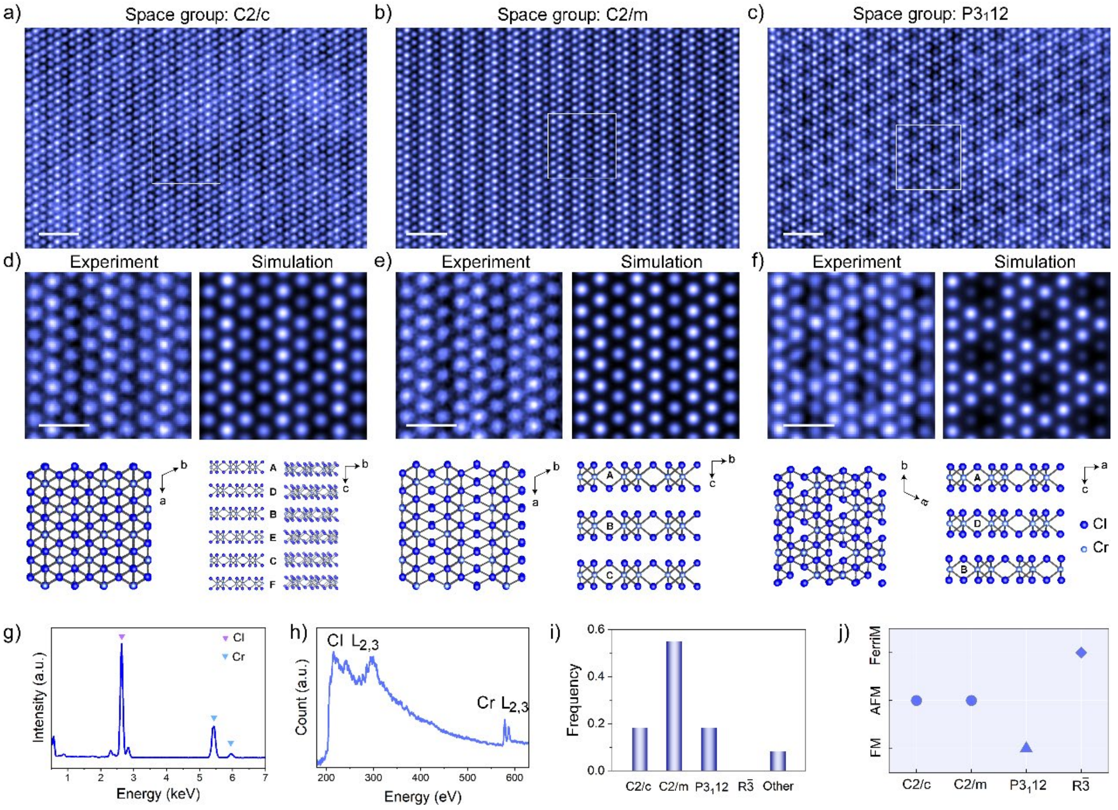

Figure 5. Atomic structures of various stacking polytypes of $CrCl_3$ a-c) Atomic-resolution ADF-STEM images showing different stacking polytypes of few-layer $CrCl_3$ crystals, consisting of C2/c, C2/m, and $P3_112$ phases from left to right, respectively. d-f) Left, enlarged STEM images in (a-c); right, the corresponding simulated images; g, h) EDS (g) and EEL (h) spectra of core-level edges of $CrCl_3$ thin film. i, j) The frequency (i) and calculated magnetic ground state (j) of different stacking polytypes. Scale bars: a-c, 2 nm; d-f, 0.5 nm.

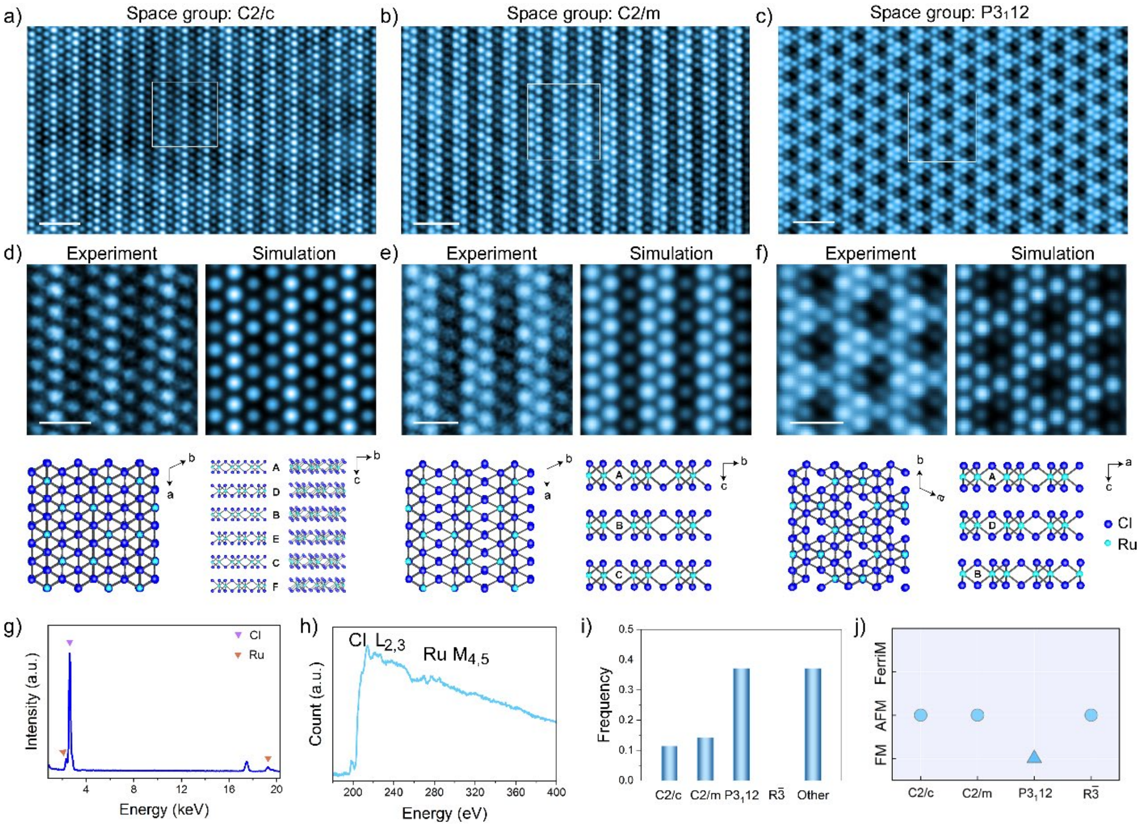

Figure 6. Atomic structures of various stacking polytypes of α-$RuCl_3$. a-c) Atomic-resolution ADF-STEM images showing different stacking polytypes of few-layer α-$RuCl_3$ crystals, consisting of C2/c, C2/m, and $P3_112$ phases from left to right, respectively. d-f) Left, enlarged STEM images in (a-c); right, the corresponding simulated images; g, h) EDS (g) and EEL (h) spectra of core-level edges of the α-$RuCl_3$ thin film. i, j) The frequency (i) and calculated magnetic ground state (j) of different stacking polytypes. Scale bars: a-c, 2 nm; d-f, 0.5 nm.

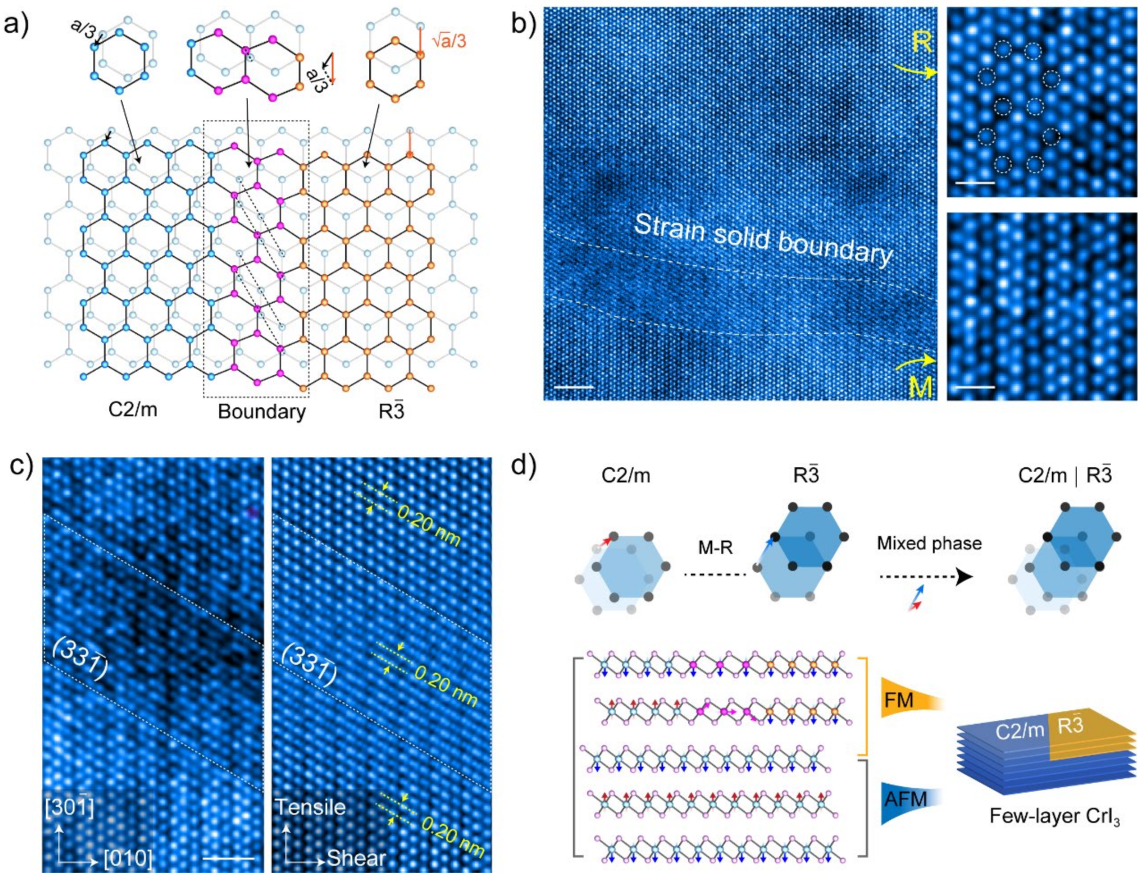

Figure 7. Strain soliton boundaries in few-layer CrI_3. Atomic-resolution ADF-STEM images of monoclinic-rhombohedral (M-R) domain boundaries, exhibiting interlayer shear and tensile strain. a) A schematic of stacking across a domain boundary. Three main bilayer Cr-network stacking configurations are shown (C2/m, boundary, and $R\bar{3}$ stacking, respectively). From left to right, the teal lattice translates left downward (zigzag direction), whereas the orange lattice moves downward (armchair direction), completing *a*/3-length translation from M to R stacking. b) Atomic-resolution ADF-STEM image showing an M-R boundary in CrI_3. The enlarged images of the M and R stacking phases are depicted in the right panel. c) The enlarged STEM image of the R-M boundary and the corresponding inverse fast Fourier transforms (IFFT) image. d) The lateral shifts of a top layer relative to a lower layer give M-R type stacking configuration along in-plane

armchair and zigzag direction translation. The magnetic order in few-layer CrI_3 with mixed stackings is depicted in the below panel. Scale bars: b, 2 nm; b-right, 0.5 nm; c, 1 nm.

Table 1 Summary of stacking structures and correlated magnetic ground states

Phases	C2/m	R$\bar{3}$	C2/c	P$3_1$12	C2/m_In	C2/c_In
CrI_3	AFM	FM	AFM	AFM	FM	FM
$CrBr_3$	FM	FM	/	/	/	/
$CrCl_3$	AFM	FerriM	AFM	FM	FM	FM
$RuCl_3$	AFM	AFM	AFM	FerriM	FerriM	FerriM

The dominant phases in MX_3 were indicated by green.

Table of Contents

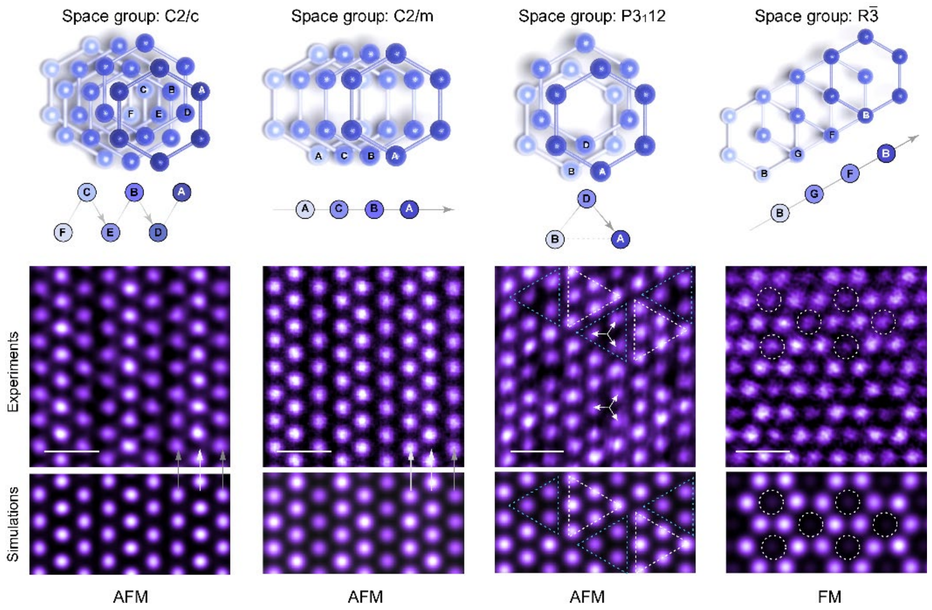

TOC: Stacking polytypes including a new monoclinic C2/c phase of 2D MX_3 generated by interlayer sliding was revealed at atomic precision. The magnetic properties of 2D MX_3 are modulated primarily by stacking engineering.